Synsint Research Group

Available online at www.synsint.com

Synthesis and Sintering

ISSN 2564-0186 (Print), **ISSN** 2564-0194 (Online)

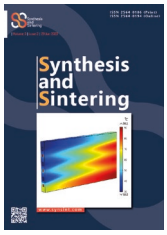

Research article

Effects of pH and calcination temperature on gel-combustion synthesizability of $BaZr_{0.8}Y_{0.2}O_3$ perovskite

Mohammad Reza Foroughi, Zahra Khakpour *, Amir Maghsoudipour

Ceramics Department, Materials and Energy Research Center (MERC), Karaj, Iran

A B S T R A C T

Solid oxide fuel cells with their advantages such as high efficiency are now considered as efficient power generation equipment. Because of its proton conductivity, perovskite is used in ceramic fuel cell electrolyte, and the addition of dopant can improve its proton conductivity. In this research, $BaZr_{0.8-x}Sr_xY_{0.2}O_3$ (x=0, 0.05, 0.1, and 0.15) perovskites were synthesized by gel-combustion method. Barium nitrate, zirconium nitrate, yttrium nitrate, and strontium nitrate were used as raw materials. Based on DTA and TGA analyses, the required temperature for calcination was determined to be around 1000 °C. XRD and FTIR analyses were used to identify the phases. The synthesis was carried out under different conditions and the effects of pH and dopant percentage on the morphology and size of the particles were investigated by FESEM. The sintering process was completed at different temperatures and a relative density of 94% was obtained at 1470 °C.

KEYWORDS

Gel-combustion synthesis
Perovskite
X-ray diffraction
Sintering
Dopant

OPEN ACCESS

1. Introduction

Fuel cells work like batteries, but unlike batteries, as long as fuel is supplied to them, they do not fail and do not need to be recharged [1, 2]. Fuel cells convert the chemical potential of hydrogen into electrical energy and its by-product is water and heat [3–5]. Solid oxide fuel cells are one of the most efficient devices that have been proposed so far for the direct conversion of chemical energy into electrical energy [6–8]. A new type of fuel cell has the ability to pass hydrogen ions, which is called "proton-conducting solid oxide fuel cell" and is based on a ceramic electrolyte material that conducts protons [9, 10].

After research conducted by Iwahara et al. [11] in 1981, the ability of proton-conducting in perovskites, a large family among oxide compounds with the general formula of ABO_3, was reported based on $SrCeO_3$. Later, in 1996, Iwahara [12] investigated the proton conductivity of a number of perovskite compounds and reported the high proton conductivity of barium-based perovskite compounds. Shortly after, in 1999, Kreuer [13] scrutinized the proton conduction mechanisms in $BaZrO_3$ and $BaCeO_3$ perovskites, which show good proton conduction, and proposed some mechanisms. Further, a lot of research was done on $BaZrO_3$ and $BaCeO_3$ perovskite compounds and it was found that although the proton conductivity of $BaCeO_3$ is higher than $BaZrO_3$, the chemical stability of $BaZrO_3$ is much higher [14–18].

In order to achieve an electrolyte with acceptable proton conductivity and chemical stability, many research works are being carried out. Proton conductivity and chemical stability of the compositions $BaCe_{0.8-x}Zr_xY_{0.2}O_{3-\delta}$ ($0<x<0.8$) were investigated and it was determined that with increasing the amount of x, the chemical stability of the composition increases and finally, the $BaCe_{0.3}Zr_{0.5}Y_{0.2}O_{3-\delta}$ compound was introduced a suitable candidate for use in proton-conducting ceramic fuel cell electrolytes [19]. In addition, $BaCe_{0.9-x}Zr_xY_{0.1}O_{3-\delta}$ ($0<x<0.9$) compositions were studied and $BaCe_{0.3}Zr_{0.6}Y_{0.1}O_{3-\delta}$ compound was disclosed as a composition with high chemical stability and acceptable proton conductivity [20]. Also, the chemical stability and proton conductivity of the $BaCe_{0.45}Zr_{0.45}Sc_{0.1}O_{3-\delta}$ compound were investigated and reported [21].

It was shown that the $BaZr_{0.8}Y_{0.2}O_{3-\delta}$ perovskite has good chemical stability up to a temperature of 1250 °C [22]. In research conducted on

* Corresponding author. *E-mail address:* z.khakpour@merc.ac.ir (Z. Khakpour)

Received 3 May 2023; Received in revised form 22 June 2023; Accepted 25 June 2023.

https://doi.org/10.53063/synsint.2023.32153

the $BaCe_{0.8-x}Zr_xY_{0.2}O_{3-\delta}$ ($0<x<0.8$), it was verified that by increasing the amount of x, the stability of perovskite increases but its sinterability decreases [23]. The effects of Gd and Nb dopants on $BaCe_{0.9-x}Zr_xM_{0.1}O_{3-\delta}$ perovskites were investigated and it was shown that the type of dopant is effective to achieve the highest chemical stability [24]. The Influences of Pr, Sn, In, and Zn dopants on the sinterability and proton conductivity of $BaZr_{0.8}Y_{0.2}O_{3-\delta}$ perovskites were studied and the highest proton conductivity was obtained with In dopant [25]. Usually, dopants are selected from the group of lanthanides or cations that have a valence of three. Also, if dopant is a rare earth element, it should not be added more than 0.2%. In choosing a dopant, in addition to capacity, its size is also important and effective, so that the greater the difference in the size of the radius, the lower the tendency to substitute and the greater the tendency for the dopant to be interstitial. For this purpose, cations with a radius close to Zr are selected in order to prevent interstitial placement [26, 27].

Various techniques have been used for the synthesis of perovskites [28], including solid-state (mechanical ball-milling [29, 30], and high energy ball-milling [31, 32]), liquid-state (auto-combustion [33, 34], sol-gel [35, 36], and co-precipitation [37–41]), and gas-state (laser ablation [42], thermal evaporation [43], molecular beam epitaxy [44], chemical vapor deposition [45], magnetron sputtering [46], DC sputtering [47], and electron beam evaporation [48]) methods.

In addition to the above-mentioned extensive research that has been published about the synthesis of perovskites, due to the low sinterability of $BaZrO_3$, several research studies have also been conducted to overcome this problem [49–52]. For instance, the $BaZr_{0.8}Y_{0.2}O_{3-\delta}$ perovskite was sintered at a temperature of 1670 °C for 24 h, and the relative density was reached to about 97% [53]. Among the other activities carried out to achieve high density at minimum sintering temperature and time, the $BaZr_{0.8}Y_{0.2}O_{3-\delta}$ perovskite was sintered by the spark plasma sintering, but the graphite phase was observed in the perovskite structure [54]. It is worth mentioning that dopants and additives have an important role in the sintering of oxide ceramics and their characteristics [55–59].

In this paper, $BaZr_{0.8-x}Sr_xY_{0.2}O_3$ (x=0, 0.05, 0.1, and 0.15) perovskites are synthesized by the gel-combustion method and then sintered at different temperatures. Characterizations are carried out using several analyses such as XRD, DTA, TGA, FTIR, and FESEM, and the effects of pH and Sr dopant percentage on the morphology and size of the particles are studied.

2. Experimental procedure

2.1. Materials and methods

In this research, the synthesis of perovskite was carried out by the gel-combustion method. Also, samples with strontium dopant, which replaces zirconium in the perovskite structure, were synthesized. In Table 1, the used raw materials are presented, and it should be noted that their high purity is important and necessary in the synthesis process.

To carry out the synthesis process, first, the stoichiometric molar ratios of each of the raw materials were calculated to reach the desired perovskite composition. Nitrate raw materials were dissolved in double distilled water with calculated stoichiometric molar ratios. The lower the amount of distilled water added, the less the problems of drying the final gel and the less time it takes to dry the gel. Since metal salts easily dissolve in water, nitrate raw materials were used.

Table 1. Specifications of raw materials.

Material	Chemical formula	Purity (%)	Supplier
Zirconium nitrate	$ZrO(NO_3)_2.xH_2O$	99.9	Sigma-Aldrich (USA)
Barium nitrate	$Ba(NO_3)_2$	99.9	Merck (Germany)
Yttrium nitrate	$Y(NO_3)_3.6H_2O$	99.9	Merck (Germany)
Strontium nitrate	$Sr(NO_3)_2$	99.9	Merck (Germany)
Citric acid	$C_6H_8O_7$	25	Merck (Germany)
Ammonia	NH_3	25	Merck (Germany)

After dissolving each powder in distilled water separately, they were placed on a hot plate with a magnetic stirrer for 30 min at a temperature of 70 °C until the solution became completely clear. After the raw materials were completely dissolved in distilled water, they were added together and completely dissolved at 70 °C for 30 min. Then citric acid was dissolved in double distilled water and added to the solution. By adding acid to the solution, the pH decreased drastically and became almost 0.8. When the solution is acidic, barium precipitates and separates from the solution. The separation of barium from the solution and its removal from the formed complex causes the $BaZrO_3$ phase to not be completely formed, and as a result, in addition to removed barium, zirconium, and yttrium are also removed from the compound in the same molar amount. In order to prevent the precipitation of barium, pH should be controlled; hence, ammonia was used to increase the pH of the solution.

The synthesis process was carried out in different pH conditions to compare the results and select the optimal conditions. For this purpose, four synthesis tests were conducted at pH 0.8 without adding ammonia, as well as pH 8, 10, and 12 with adding ammonia. After adding

Table 2. The coding/naming of synthesized samples in different conditions.

Sample code	Molar ratio of cations to citric acid	pH	Composition	Remarks
A	1:2	8	$BaZr_{0.8}Y_{0.2}O_3$	NH_3 was added.
B	1.1:5	8	$BaZr_{0.8}Y_{0.2}O_3$	NH_3 was added.
C	1:2	0.8	$BaZr_{0.8}Y_{0.2}O_3$	NH_3 was not added.
D	1:2	10	$BaZr_{0.8}Y_{0.2}O_3$	NH_3 was added.
E	1:2	12	$BaZr_{0.8}Y_{0.2}O_3$	NH_3 was added.
F	1:2	10	$BaZr_{0.75}Sr_{0.05}Y_{0.2}O_3$	NH_3 and Sr were added.
G	1:2	10	$BaZr_{0.7}Sr_{0.1}Y_{0.2}O_3$	NH_3 and Sr were added.
H	1:2	10	$BaZr_{0.65}Sr_{0.15}Y_{0.2}O_3$	NH_3 and Sr were added.

ammonia and controlling pH, each solution was stirred for 24 h at 100 °C to form the complex. With the passage of time and the release of water, the gel was formed, which was dried by placing in a dryer at 150 °C for 24 h to produce the powder. The synthesis was performed with different proportions of citric acid i.e., in two molar ratios of total cations to citric acid of 1.1:5 and 1:2. According to the synthesis parameters, pH and citric acid ratio, the names of the studied samples are based on Table 2. After synthesizing the sample and drying the obtained gel, a black powder was produced, which turned white after calcination. The powder calcination process was carried out at temperatures of 1000, 1100, and 1200 °C with a heating rate of 10 °C/min for 2 h. To name the samples, numbers 1 to 4 were used after the code of each sample so that in front of the codes, number 1 before calcination, number 2 after calcination at 1000 °C, number 3 after calcination at 1100 °C, and number 4 after calcination at 1200 °C was placed.

After calcination of the powders, pellets were prepared by uniaxial pressing, and carboxymethyl cellulose glue (7 wt%) was used for granulation to improve the strength of the pellets. Actually, after the complete mixing of glue and powder and 24 hours of holding time, the formed granules were ready to press. The pressing was done in a mold with a diameter of 10 mm and an applied pressure of 200 MPa. The thickness of the obtained pellets was ~3 mm, and after drying in an oven at 150 °C for 24 h, they were ready for sintering. The sintering process was carried out in the box furnace (Exciton Azar 1250) at temperatures of 1300, 1400, and 1470 °C for 6 h with a heating rate of 5 °C/min to clarify the effect of sintering temperature on the final properties.

2.2. Characterization

An Olympus BX61 light microscope was used to observe the powder size. To investigate the thermal behavior of the powders, a simultaneous thermal analysis (STA: PL-STA-1640) device was used. For phase analysis, an XRD facility (Philips DW-3710) was employed using CuK_{α} radiation with a wavelength of 1.5404 Å for all experiments. The time-per-step was 1 s, the step size was 0.02 degrees, and the scanning range was between 20 and 80 degrees. A Cambridge S360 (SEM) and a Mira3 Tescan (FESEM) were used to characterize the microstructures of powders and samples. To prepare the sample for microscopic examination, some of the powder was dispersed in deionized water. Then, a drop of it was placed on a microscope slide and after drying, its surface was coated with gold. The surface of the sintered pellets was also prepared for SEM observation using sandpapers (No. 1000, 1200, 1500, and 2000) for polishing and then coating with a layer of gold. For Fourier transform-infrared (FTIR) spectroscopy, a Perkin Elmer spectrum RX1 device was used in the wave number range of 400–4000 cm^{-1}. The density of sintered samples was calculated by Archimedes' method.

3. Results and discussion

First, the synthesis of sample A (based on the conditions mentioned in Table 2) was done. After drying the synthesized powder, simultaneous thermal analysis was performed to select the minimum calcination temperature, the results of which can be seen in Fig. 1. According to the changes in the slope of the thermogravimetric (TG) diagram, black color, and the critical points in the differential thermal analysis (DTA) curve, red color, it is concluded that in the temperature range of 0–200 °C, physical water is absorbed, and structural water evaporates. The endothermic peak in the temperature range of 200–250 °C indicates the release of NO_x compounds (approximate temperature 210 °C). In the range of 250–470 °C, two exothermic peaks can be seen as a result of the decomposition of oxides. About 70% of weight loss occurs in this temperature range. In the range of 470–700 °C, decomposition of carbonate materials takes place. At the temperature of 560 °C, perovskite crystallization (exothermic peak) takes place. In the range of 700–1150 °C, carbonates continue to decompose. After the temperature of 1000 °C, the slope of the TG diagram is almost constant, and no weight loss is observed. The selected calcination temperature is chosen higher than this temperature by interpreting the STA results. Therefore, according to the stability of the slope of the thermogravimetric diagram after the temperature of 1000 °C, this temperature is selected for calcination of the sample.

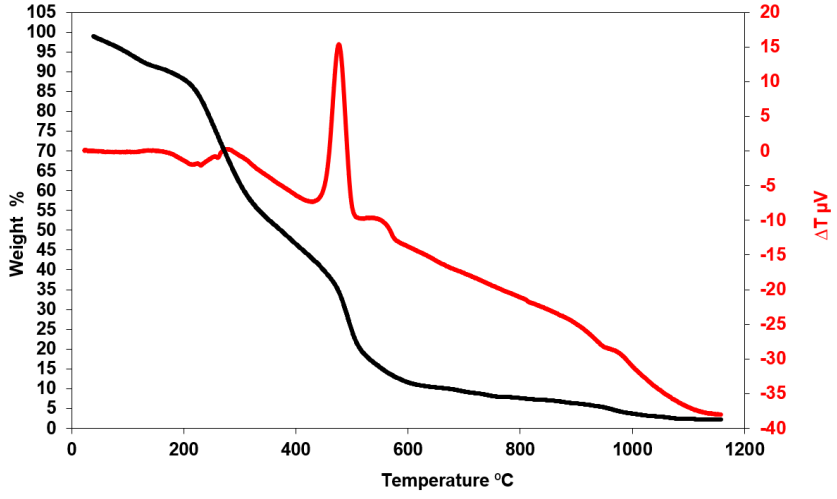

Fig. 1. STA results of synthesized sample A.

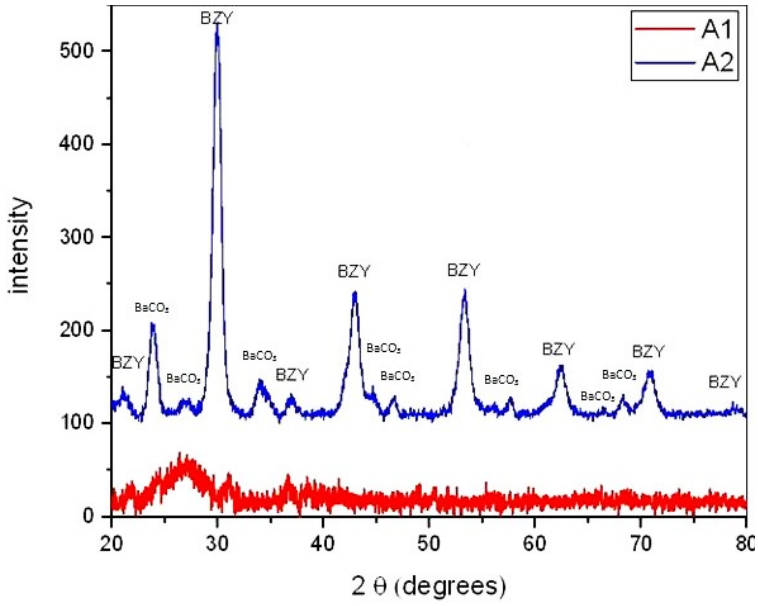

Fig. 2. XRD results of sample A1 (before calcination) and sample A2 (after calcination at 1000 °C).

The results of XRD analysis on sample A (before and after calcination at 1000 °C for 2 h) are shown in Fig. 2. As expected after the synthesis by gel-combustion method, no peaks related to crystallinity can be seen in the XRD spectrum because the powder is amorphous. The results of the STA test (Fig. 1) also confirmed that crystallization takes place at a temperature of about 560 °C. Therefore, the powder that has been heated to a temperature of 150 °C has not yet crystallized. However, after calcination at 1000 °C, some crystalline peaks attributed to perovskite phase $BaZr_{0.8}Y_{0.2}O_3$ (BZY) were revealed. Several peaks belonging to the barium carbonate ($BaCO_3$) were also detected.

To reconfirm the $BaCO_3$ phase observed in the XRD analysis, the FTIR test was also taken. Fig. 3 shows the results of sample A after calcination at 1000 °C. By comparing the wave numbers reported in the literature [60], it is seen that the values are almost the same.

The temperature range of decomposition of barium carbonate is 1050–1150 °C [61]. Therefore, this phase does not disappear at the calcination temperature of 1000 °C. Hence, it is necessary to increase the calcination temperature. For this purpose, the calcination of the sample was also done at the temperatures of 1100 and 1200 °C, and the results obtained from the XRD test can be seen in Fig. 4. As can be

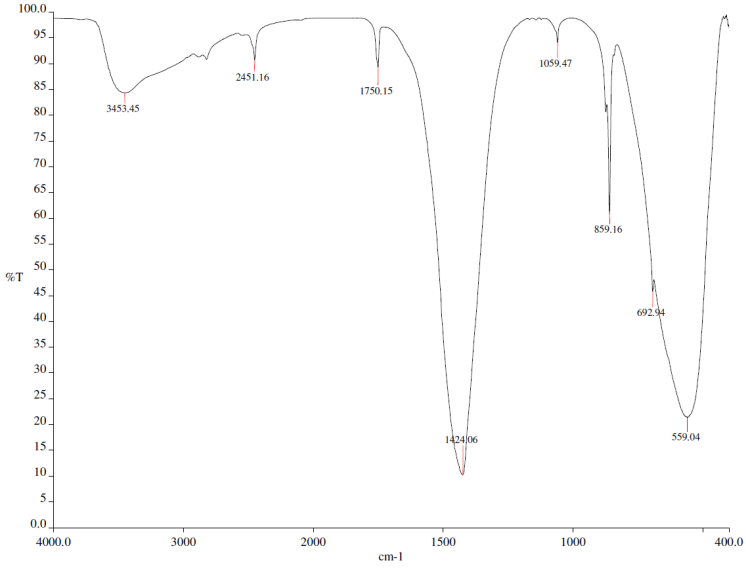

Fig. 3. FTIR results of sample A after calcination at 1000 °C.

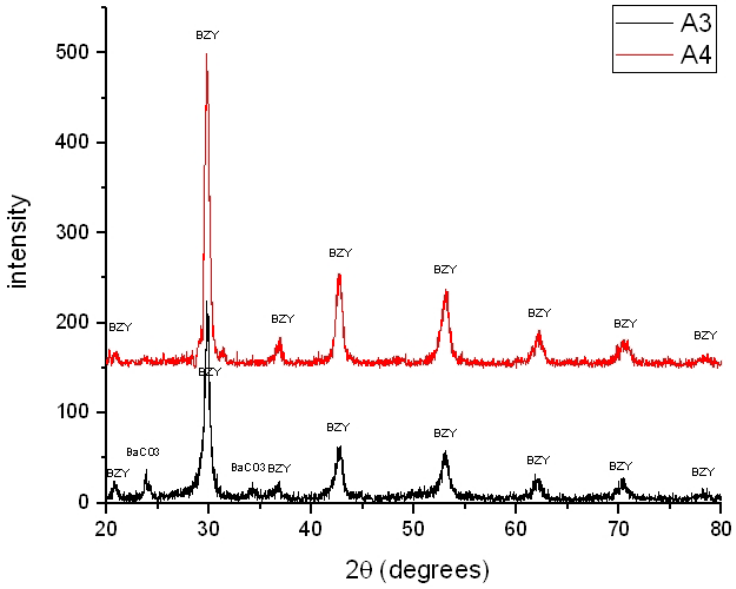

Fig. 4. XRD results of samples A3 and A4 after calcination at 1100 and 1200 °C, respectively.

seen, when the calcination is done at 1100 °C, the number of $BaCO_3$ peaks decreases, but this phase is still observed. If calcination is performed at 1200 °C, only perovskite peaks are identified, and no trace of barium carbonate is detected.

According to the used raw materials, the only source of carbon supply for the formation of barium carbonate is citric acid. The presence of citric acid is also necessary for the formation of a complex. The synthesis process of sample B was done with a lower proportion of citric acid in order to investigate the effect of reducing the amount of citric acid in the formation of the barium carbonate phase. In Fig. 5, the results obtained from the XRD analysis of B samples can be seen. In the XRD spectrum before calcination, crystalline peaks are observed. Since perovskite crystallization takes place at about 560 °C, therefore, the observed peaks cannot be related to this phase. In synthesized sample B, unwanted intermediate phases of barium carbonate and unreacted raw materials of barium nitrate are observed. After

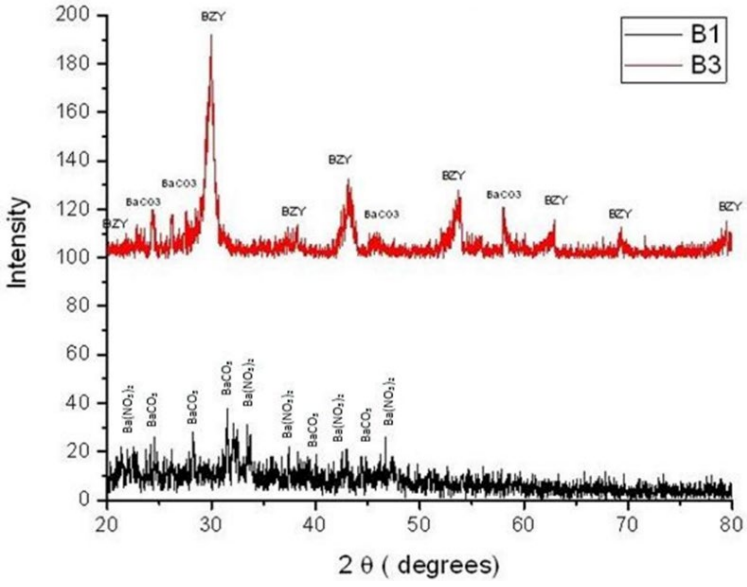

Fig. 5. XRD results of sample B1 (before calcination) and sample B3 (after calcination at 1100 °C).

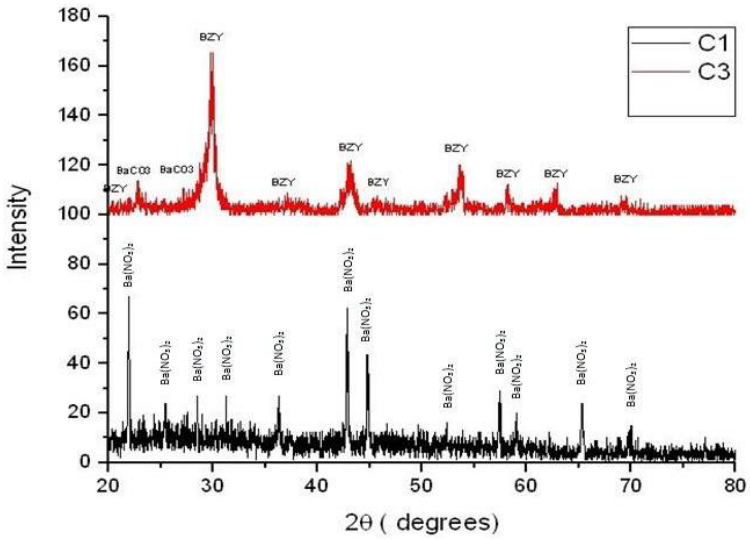

Fig. 6. XRD results of sample C1 (before calcination) and sample C3 (after calcination at 1100 °C).

calcination at 1100 °C, the peaks of barium carbonate phase are still detected by the XRD analysis. Therefore, it can be said that by reducing the amount of citric acid, the formation of the barium carbonate phase cannot be prevented, and the only way to remove this phase seems to be calcination at 1200 °C.

After investigating the effect of the amount of citric acid, the value of pH is studied. First, for the synthesis of sample C, ammonia was not added to avoid changing the pH of the solution. The pH of the solution was approximately 0.8 using. Fig. 6 shows the results obtained from the XRD analysis of samples C. If the synthesis is done at low pH, the crystalline peaks corresponding to the barium nitrate phase are identified. Due to the low pH, there is no necessary adhesion between the Ba^{2+} ions, therefore, unreacted barium nitrate is seen. Even after calcination at 1100 °C, traces of barium carbonate can be observed.

In the synthesis of samples D and E, the pH of the solutions is increased to 10 and 12, respectively, by adding ammonia. The results obtained from XRD analysis on samples D and E can be seen in Figs. 7 and 8, respectively. After the synthesis of sample D at the calcination

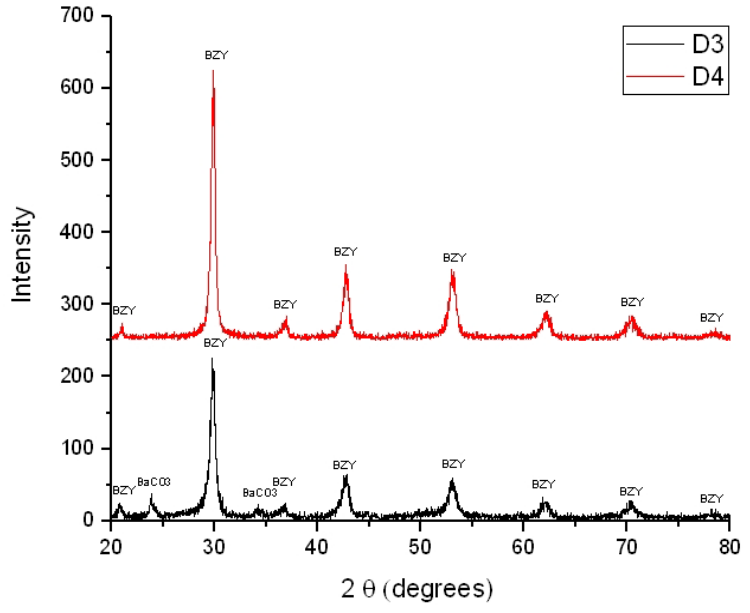

Fig. 7. XRD results of sample D3 (after calcination at 1100 °C) and sample D4 (after calcination at 1200 °C).

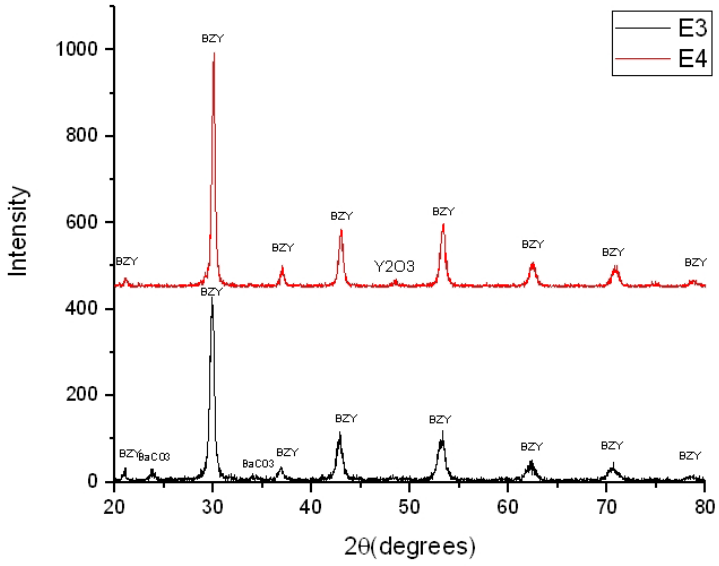

Fig. 8. XRD results of sample E3 (after calcination at 1100 °C) and sample E4 (after calcination at 1200 °C).

temperature of 1100 °C, the peaks related to the barium carbonate are observed, but at the calcination temperature of 1200 °C, only the peaks of the perovskite phase are detected. After the synthesis of sample E at the calcination temperature of 1100 °C, peaks related to barium carbonate can also be seen. At the calcination temperature of 1200 °C, although the peaks attributed to barium carbonate are removed, a peak related to yttrium oxide appears. This observation shows that not only barium compounds are precipitated from the solution at low pH, but also the yttrium oxide phase is separated at high pH, so the pure perovskite phase is no longer obtained.

FESEM was used to observe the morphology and particle size of some synthesized powders, which are shown in Fig. 9. From these nano-scale images, it can be concluded that with increasing pH, the average size of powder particles increases.

According to the results of XRD and FESEM analyses, the next samples were produced at the ρH of 10. To observe the effect of strontium dopant, new perovskites were synthesized based on the compounds designed in Table 2. The XRD results of samples F, G, and H are shown in Fig. 10 and the FESEM image of the synthesized powder of sample G4 is presented in Fig. 11. As known from the synthesis of sample H, when the amount of strontium dopant is 0.15 mol%, the peaks related to the yttrium oxide appear. In the

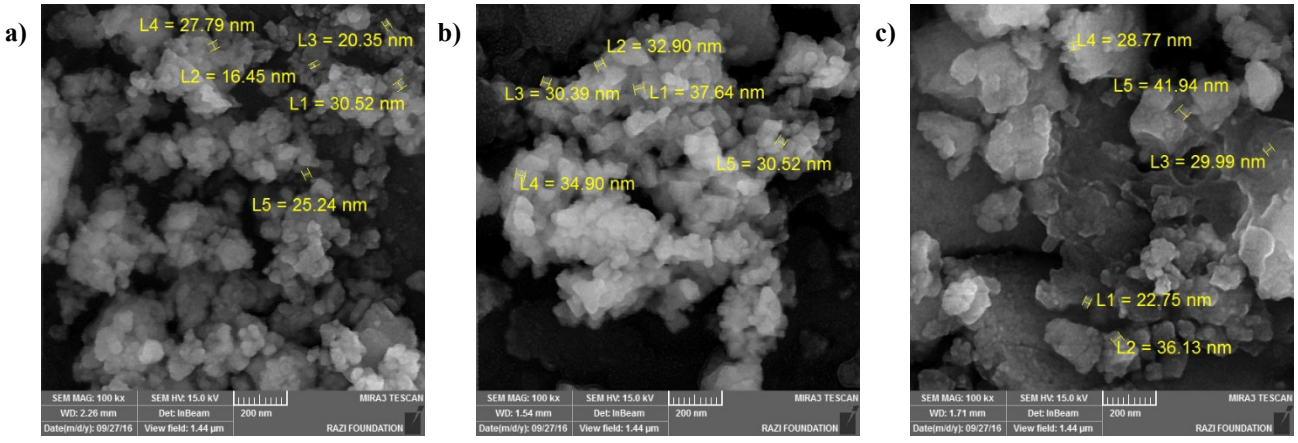

Fig. 9. FESEM images of the synthesized powders after calcination at 1200 °C: a) sample A4 (pH: 8), b) sample D4 (pH: 10), and c) sample E4 (pH: 12).

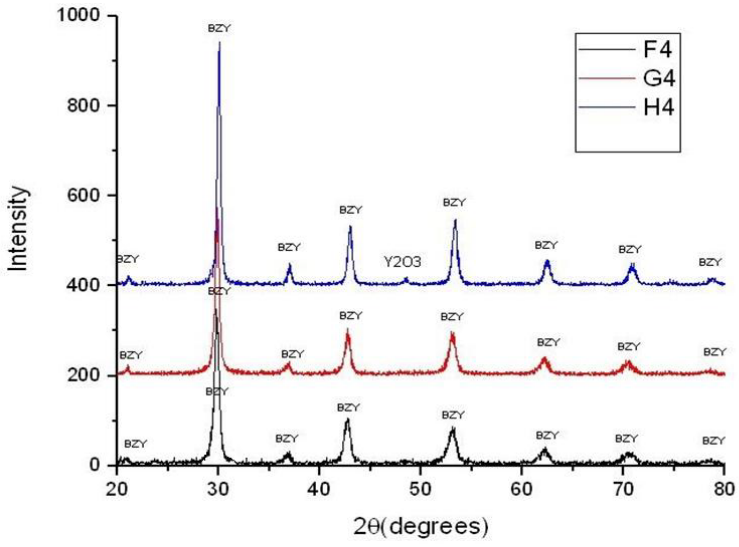

Fig. 10. XRD results of samples F, G, and H (after calcination at 1200 °C).

synthesis of samples F (doped with 0.05 mol% Sr) and G (doped with 0.1 mol% Sr), only peaks attributed to the perovskite phase are evident. Increasing the pH increases the rate of the reaction and finally the released heat increases. Therefore, in conditions where the pH of the solution is high, it leads to the formation of intermediate phases. In the synthesis of sample H with a pH of 12, the phase of yttrium oxide is seen. From the comparison of FESEM images in Figs. 9 and 11, it can be concluded that by adding the Sr dopant, the average size of the synthesized powder particles increases.

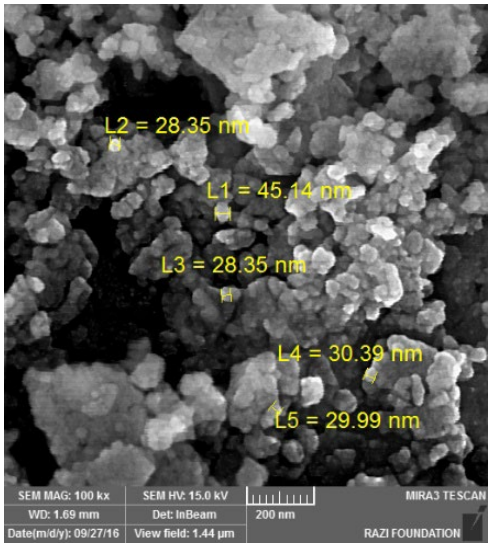

Fig. 11. FESEM image of the synthesized Sr-doped G4 sample powders (after calcination at 1200 °C).

After calcination and tablet preparation, the sintering process was carried out at the temperatures of 1300, 1400, and 1470 °C for 6 h with a heating rate of 5 °C/min. In Table 3, the relative density obtained after sintering at each temperature for various perovskite compounds is reported. As it can be clearly recognized, with the increase of the sintering temperature, the final density increases. At the temperature of 1470 °C, a relative density of 94.2% was obtained in the $BaZr_{0.8}Y_{0.2}O_3$ sample. In all selected temperatures for sintering, the density has decreased with the increase in the amount of strontium dopant. The SEM images of the samples sintered at 1470 °C are shown in Fig. 12. By increasing the amount of Sr dopant, the average particle size increases. It seems that in sample H4, the size of particles is below 500 nm, while particles with size below 200 nm are observed in sample D4.

Table 3. Relative densities of samples with different compositions and sintering temperatures.

Composition	Sintering temperature		
	1300 °C	1400 °C	1470 °C
$BaZr_{0.8}Y_{0.2}O_3$	83.9%	90.1%	94.2%
$BaZr_{0.75}Sr_{0.05}Y_{0.2}O_3$	83.1%	88.8%	94.0%
$BaZr_{0.7}Sr_{0.1}Y_{0.2}O_3$	83.1%	88.7%	93.6%
$BaZr_{0.65}Sr_{0.15}Y_{0.2}O_3$	82.4%	86.4%	93.5%

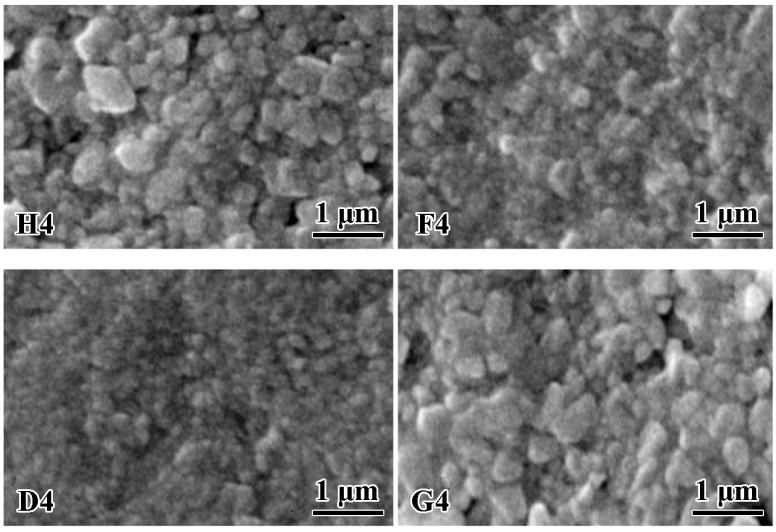

Fig. 12. SEM images of the sintered tablets at 1470 °C.

4. Conclusions

In this research, several perovskite compounds were synthesized. For this purpose, the solution containing nitrate-citrate ions was turned into spongy ash via a combustion reaction and after turning into a gel with high viscosity, which finally led to the formation of nano powder. The XRD pattern of sample A before calcination showed an amorphous phase, but crystalline peaks were observed in samples B and C before calcination. In sample B, unwanted intermediate phases and unreacted raw materials were observed. Moreover, due to the low pH in sample C, there was no adhesion for Ba^{2+}, and hence, unreacted raw materials were seen. Barium carbonate was observed in the XRD results of all samples processed under different conditions up to the calcination temperature of 1100 °C, and the only way to eliminate that phase was to increase the calcination temperature. In the XRD pattern of the sample synthesized at pH of 12 at the calcination temperature of 1200 °C, the yttrium oxide phase was identified. Increasing pH enhanced the reaction rate and released heat, which led to the formation of intermediate phases. In the conditions where the amount of Sr dopant increased to 0.15 mol%, peaks related to yttrium oxide were detected in the XRD pattern after calcination at 1200 °C. In addition, with the increase of dopant, the crystallite size increased. By increasing the amount of Sr dopant, the average particle size in the sintered samples increased.

CRediT authorship contribution statement

Mohammad Reza Foroughi: Data curation, Investigation, Writing – original draft.

Zahra Khakpour: Conceptualization, Funding acquisition, Methodology, Project administration, Supervision, Writing – review & editing.

Amir Maghsoudipour: Funding acquisition, Methodology, Supervision.

Data availability

The data underlying this article will be shared on reasonable request to the corresponding author.

Declaration of competing interest

The authors declare no competing interests.

Funding and acknowledgment

The paper is derived from the first author's master's thesis. The authors would like to express their gratitude to the Materials and Energy Research Center for its support of this research project.

References

[1] M. Winter, R.J. Brodd, What are batteries, fuel cells, and supercapacitors?, Chem. Rev. 104 (2004) 4245–4270. https://doi.org/10.1021/cr020730k.

[2] Z.P. Cano, D. Banham, S. Ye, A. Hintennach, J. Lu, et al., Batteries and fuel cells for emerging electric vehicle markets, Nat. Energy. 3 (2018) 279–289. https://doi.org/10.1038/s41560-018-0108-1.

[3] Z. Wang, X. Zhang, A. Rezazadeh, Hydrogen fuel and electricity generation from a new hybrid energy system based on wind and solar energies and alkaline fuel cell, Energy Rep. 7 (2021) 2594–2604. https://doi.org/10.1016/j.egyr.2021.04.060.

[4] A.B. Stambouli, Fuel cells: The expectations for an environmental-friendly and sustainable source of energy, Renew. Sustain. Energy Rev. 15 (2011) 4507–4520. https://doi.org/10.1016/j.rser.2011.07.100.

[5] A. Sartbaeva, V.L. Kuznetsov, S.A. Wells, P.P. Edwards, Hydrogen nexus in a sustainable energy future, Energy Environ. Sci. 1 (2008) 79. https://doi.org/10.1039/b810104n.

[6] J. Milewski, J. Zdeb, A. Szczęśniak, A. Martsinchyk, J. Kupecki, O. Dybiński, Concept of a solid oxide electrolysis-molten carbonate fuel cell hybrid system to support a power-to-gas installation, Energy Convers. Manag. 276 (2023) 116582. https://doi.org/10.1016/j.enconman.2022.116582.

[7] M. Shen, F. Ai, H. Ma, H. Xu, Y. Zhang, Progress and prospects of reversible solid oxide fuel cell materials, IScience. 24 (2021) 103464. https://doi.org/10.1016/j.isci.2021.103464.
[8] K.A. Kuterbekov, A.V. Nikonov, K.Z. Bekmyrza, N.B. Pavzderin, A.M. Kabyshev, et al., Classification of solid oxide fuel cells, Nanomaterials. 12 (2022) 1059. https://doi.org/10.3390/nano12071059.
[9] M.B. Hanif, S. Rauf, M. Motola, Z.U.D. Babar, C.-J. Li, C.-X. Li, Recent progress of perovskite-based electrolyte materials for solid oxide fuel cells and performance optimizing strategies for energy storage applications, Mater. Res. Bull. 146 (2022) 111612. https://doi.org/10.1016/j.materresbull.2021.111612.
[10] S. Hossain, A.M. Abdalla, S.N.B. Jamain, J.H. Zaini, A.K. Azad, A review on proton conducting electrolytes for clean energy and intermediate temperature-solid oxide fuel cells, Renew. Sustain. Energy Rev. 79 (2017) 750–764. https://doi.org/10.1016/j.rser.2017.05.147.
[11] H. Iwahara, T. Esaka, H. Uchida, N. Maeda, Proton conduction in sintered oxides and its application to steam electrolysis for hydrogen production, Solid State Ion. 3–4 (1981) 359–363. https://doi.org/10.1016/0167-2738(81)90113-2.
[12] H. Iwahara, Proton conducting ceramics and their applications, Solid State Ion. 86–88 (1996) 9–15. https://doi.org/10.1016/0167-2738(96)00087-2.
[13] K. Kreuer, Aspects of the formation and mobility of protonic charge carriers and the stability of perovskite-type oxides, Solid State Ion. 125 (1999) 285–302. https://doi.org/10.1016/S0167-2738(99)00188-5.
[14] K. Katahira, Y. Kohchi, T. Shimura, H. Iwahara, Protonic conduction in Zr-substituted BaCeO3, Solid State Ion. 138 (2000) 91–98. https://doi.org/10.1016/S0167-2738(00)00777-3.
[15] S.V. Bhide, A.V. Virkar, Stability of BaCeO3-based proton conductors in water-containing atmospheres, J. Electrochem. Soc. 146 (1999) 2038−2044. https://doi.org/10.1149/1.1391888.
[16] X. Ma, J. Dai, H. Zhang, D.E. Reisner, Protonic conductivity nanostructured ceramic film with improved resistance to carbon dioxide at elevated temperatures, Surf. Coat. Technol. 200 (2005) 1252–1258. https://doi.org/10.1016/j.surfcoat.2005.07.099.
[17] A. D'Epifanio, E. Fabbri, E. Di Bartolomeo, S. Licoccia, E. Traversa, Design of BaZr0.8Y0.2O3–δ protonic conductor to improve the electrochemical performance in intermediate temperature solid oxide fuel cells (IT-SOFCs), Fuel Cells. 8 (2008) 69–76. https://doi.org/10.1002/fuce.200700045.
[18] J. Lu, L. Wang, L. Fan, Y. Li, L. Dai, H. Guo, Chemical stability of doped BaCeO3-BaZrO3 solid solutions in different atmospheres, J. Rare Earths. 26 (2008) 505–510. https://doi.org/10.1016/S1002-0721(08)60127-1.
[19] E. Fabbri, A. Depifanio, E. Dibartolomeo, S. Licoccia, E. Traversa, Tailoring the chemical stability of Ba(Ce0.8−xZrx)Y0.2O3−δ protonic conductors for Intermediate Temperature Solid Oxide Fuel Cells (IT-SOFCs), Solid State Ion. 179 (2008) 558–564. https://doi.org/10.1016/j.ssi.2008.04.002.
[20] Z. Zhong, Stability and conductivity study of the BaCe0.9−xZrxY0.1O2.95 systems, Solid State Ion. 178 (2007) 213–220. https://doi.org/10.1016/j.ssi.2006.12.007.
[21] A. Azad, J. Irvine, Synthesis, chemical stability and proton conductivity of the perovksites Ba(Ce,Zr)1−xScxO3−δ, Solid State Ion. 178 (2007) 635–640. https://doi.org/10.1016/j.ssi.2007.02.004.
[22] A. Magrez, Preparation, sintering, and water incorporation of proton conducting Ba0.99Zr0.8Y0.2O3: comparison between three different synthesis techniques, Solid State Ion. 175 (2004) 585–588. https://doi.org/10.1016/j.ssi.2004.03.045.
[23] Y. Guo, Y. Lin, R. Ran, Z. Shao, Zirconium doping effect on the performance of proton-conducting BaZryCe0.8−yY0.2O3−δ (0.0≤y≤0.8) for fuel cell applications, J. Power Sources. 193 (2009) 400–407. https://doi.org/10.1016/j.jpowsour.2009.03.044.
[24] K.H. Ryu, S.M. Haile, Chemical stability and proton conductivity of doped BaCeO3–BaZrO3 solid solutions, Solid State Ion. 125 (1999) 355–367. https://doi.org/10.1016/S0167-2738(99)00196-4.
[25] H. Bae, G.M. Choi, Novel modification of anode microstructure for proton-conducting solid oxide fuel cells with BaZr0.8Y0.2O3−δ electrolytes, J. Power Sources. 285 (2015) 431–438. https://doi.org/10.1016/j.jpowsour.2015.03.090.
[26] H. Iwahara, T. Yajima, T. Hibino, K. Ozaki, H. Suzuki, Protonic conduction in calcium, strontium and barium zirconates, Solid State Ion. 61 (1993) 65–69. https://doi.org/10.1016/0167-2738(93)90335-Z.
[27] P. Goharian, A. Aghaei, B. Eftekhari Yekta, S. Banijamali, Lithium ion conductivity, crystallization tendency, and microstructural evolution of LiZrxTi2-x(PO4)3 NASICON glass-ceramics (x = 0 - 0.4), Synth. Sinter. 3 (2023) 67–72. https://doi.org/10.53063/synsint.2023.32148.
[28] D. Kumar, R. Sagar Yadav, Monika, A. Kumar Singh, S. Bahadur Rai, Synthesis techniques and applications of perovskite materials, Perovskite Materials, Devices and Integration, IntechOpen. (2020). https://doi.org/10.5772/intechopen.86794.
[29] R. Pandey, A. Tiwari, A. Upadhyay, A.K. Singh, Phase coexistence and the structure of the morphotropic phase boundary region in (1−x)Bi(Mg1/2Zr1/2)O3–xPbTiO3 piezoceramics, Acta Mater. 76 (2014) 198–206. https://doi.org/10.1016/j.actamat.2014.05.023.
[30] I.O. Troyanchuk, N.V. Kasper, D.D. Khalyavin, H. Szymczak, R. Szymczak, M. Baran, Magnetic and electrical transport properties of orthocobaltites R0.5Ba0.5CoO3 (R = La, Pr, Nd, Sm, Eu, Gd, Tb, Dy), Phys. Rev. B. 58 (1998) 2418–2421. https://doi.org/10.1103/PhysRevB.58.2418.
[31] L. Zhang, Z. Xu, L. Cao, X. Yao, Synthesis of BF–PT perovskite powders by high-energy ball milling, Mater. Lett. 61 (2007) 1130–1133. https://doi.org/10.1016/j.matlet.2006.06.069.
[32] A. Upadhyay, R. Pandey, A.K. Singh, Origin of ferroelectric P-E loop in cubic compositions and structure of poled (1- x)Bi(Mg 1/2 Zr 1/2)O3 - x PbTiO3 piezoceramics, J. Am. Ceram. Soc. 100 (2017) 1743−1750. https://doi.org/10.1111/jace.14735.
[33] D. Kumar, C.B. Singh, N.K. Verma, A.K. Singh, Synthesis and structural investigations on multiferroic Ba1-xSrxMnO3 perovskite manganites, Ferroelectrics. 518 (2017) 191–195. https://doi.org/10.1080/00150193.2017.1360663.
[34] S. Yin, D. Chen, W. Tang, Combustion synthesis and luminescent properties of CaTiO3: Pr, Al persistent phosphors, J. Alloys Compd. 441 (2007) 327–331. https://doi.org/10.1016/j.jallcom.2006.09.120.
[35] A. Rajaeiyan, M.M. Bagheri-Mohagheghi, Comparison of sol-gel and co-precipitation methods on the structural properties and phase transformation of γ and α-Al2O3 nanoparticles, Adv. Manuf. 1 (2013) 176–182. https://doi.org/10.1007/s40436-013-0018-1.
[36] V.M. Andrade, R.J.C. Vivas, S.S. Pedro, J.C.G. Tedesco, A.L. Rossi, A.A. Coelho, D.L. Rocco, M.S. Reis, Magnetic and magnetocaloric properties of La0.6Ca0.4MnO3 tunable by particle size and dimensionality, Acta Mater. 102 (2016) 49–55. https://doi.org/10.1016/j.actamat.2015.08.080.
[37] S. Ahmadi, Synthesis and characterization of aluminum-yttrium perovskite powder using a co-precipitation technique, Synth. Sinter. 2 (2022) 170–175. https://doi.org/10.53063/synsint.2022.24135.
[38] R.-R. Pei, X. Chen, Y. Suo, T. Xiao, Q.-Q. Ge, et al., Synthesis of La0.85Sr0.15Ga0.8Mg0.2O3−δ powder by carbonate co-precipitation combining with azeotropic-distillation process, Solid State Ion. 219 (2012) 34–40. https://doi.org/10.1016/j.ssi.2012.05.022.
[39] V. Uskoković, M. Drofenik, Four novel co-precipitation procedures for the synthesis of lanthanum-strontium manganites, Mater. 28 (2007) 667–672. https://doi.org/10.1016/j.matdes.2005.07.002.
[40] T.-H. Cho, Y. Shiosaki, H. Noguchi, Preparation and characterization of layered LiMn1/3Ni1/3Co1/3O2 as a cathode material by an oxalate co-precipitation method, J. Power Sources.

159 (2006) 1322–1327. https://doi.org/10.1016/j.jpowsour.2005.11.080.
[41] A.B. Gaikwad, S.C. Navale, V. Samuel, A.V. Murugan, V. Ravi, A co-precipitation technique to prepare BiNbO4, MgTiO3 and Mg4Ta2O9 powders, Mater. Res. Bull. 41 (2006) 347–353. https://doi.org/10.1016/j.materresbull.2005.08.010.
[42] T. Imai, M.O. Masanori Okuyama, Y.H. Yoshihiro Hamakawa, PbTiO3 thin films deposited by laser ablation, Jpn. J. Appl. Phys. 30 (1991) 2163. https://doi.org/10.1143/JJAP.30.2163.
[43] Y. Li, X. Xu, C. Wang, C. Wang, F. Xie, et al., Investigation on thermal evaporated CH3NH3PbI3 thin films, AIP Adv. 5 (2015). https://doi.org/10.1063/1.4930545.
[44] Z. Yu, J. Ramdani, J.A. Curless, J.M. Finder, C.D. Overgaard, et al., Epitaxial perovskite thin films grown on silicon by molecular beam epitaxy, J. Vac. Sci. Technol. B. 18 (2000) 1653–1657. https://doi.org/10.1116/1.591445.
[45] B.S. Kwak, K. Zhang, E.P. Boyd, A. Erbil, B.J. Wilkens, Metalorganic chemical vapor deposition of BaTiO3 thin films, J. Appl. Phys. 69 (1991) 767–772. https://doi.org/10.1063/1.347362.
[46] C.J. Lu, H.M. Shen, Y.N. Wang, Preparation and crystallization of Pb(Zr 0.95 Ti 0.05)O3 thin films deposited by radio-frequency magnetron sputtering with a stoichiometric ceramic target, Appl. Phys. A. 67 (1998) 253–258. https://doi.org/10.1007/s003390050767.
[47] B. Yang, J.Y. Wang, Y.M. Jia, Y. Huang, Preparation of PbTiO3 thin film by dc single-target magnetron sputtering, International Conference on Thin Film Physics and Applications. (1991) 725. https://doi.org/10.1117/12.47277.
[48] S.R. Pae, S. Byun, J. Kim, M. Kim, I. Gereige, B. Shin, Improving uniformity and reproducibility of hybrid perovskite solar cells via a low-temperature vacuum deposition process for NiOx hole transport layers, ACS Appl. Mater. Interfaces. 10 (2018) 534–540. https://doi.org/10.1021/acsami.7b14499.
[49] J.-S. Park, J.-H. Lee, H.-W. Lee, B.-K. Kim, Low temperature sintering of BaZrO3-based proton conductors for intermediate temperature solid oxide fuel cells, Solid State Ion. 181 (2010) 163–167. https://doi.org/10.1016/j.ssi.2009.06.015.
[50] H.P. Kumar, C. Vijayakumar, C.N. George, S. Solomon, R. Jose, et al., Characterization and sintering of BaZrO3 nanoparticles synthesized through a single-step combustion process, J. Alloys Compd. 458 (2008) 528–531. https://doi.org/10.1016/j.jallcom.2007.04.032.
[51] B. Bendjeriou-Sedjerari, J. Loricourt, D. Goeuriot, P. Goeuriot, Sintering of BaZrO3 and SrZrO3 perovskites: Role of substitutions by yttrium or ytterbium, J. Alloys Compd. 509 (2011) 6175–6183. https://doi.org/10.1016/j.jallcom.2011.02.088.
[52] F.J.A. Loureiro, N. Nasani, G.S. Reddy, N.R. Munirathnam, D.P. Fagg, A review on sintering technology of proton conducting BaCeO3-BaZrO3 perovskite oxide materials for Protonic Ceramic Fuel Cells, J. Power Sources. 438 (2019) 226991. https://doi.org/10.1016/j.jpowsour.2019.226991.
[53] D. Lahiri, V. Singh, G.R. Rodrigues, T.M.H. Costa, M.R. Gallas, et al., Ultrahigh-pressure consolidation and deformation of tantalum carbide at ambient and high temperatures, Acta Mater. 61 (2013) 4001–4009. https://doi.org/10.1016/j.actamat.2013.03.014.
[54] S. Wang, Y. Liu, J. He, F. Chen, K.S. Brinkman, Spark-plasma-sintered barium zirconate based proton conductors for solid oxide fuel cell and hydrogen separation applications, Int. J. Hydrog. Energy. 40 (2015) 5707–5714. https://doi.org/10.1016/j.ijhydene.2015.02.116.
[55] M. Mansoor, M. Mansoor, M. Mansoor, Z. Er, F. Çinar Şahin, Ab-initio study of paramagnetic defects in Mn and Cr doped transparent polycrystalline Al2O3 ceramics, Synth. Sinter. 1 (2021) 135–142. https://doi.org/10.53063/synsint.2021.1340.
[56] M.K.G. Abbas, S. Ramesh, K.Y.S. Lee, Y.H. Wong, P. Ganesan, et al., Effects of sintering additives on the densification and properties of alumina-toughened zirconia ceramic composites, Ceram. Int. 46 (2020) 27539–27549. https://doi.org/10.1016/j.ceramint.2020.07.246.
[57] A. Khan, A. Ali, I. Khan, Sintering behavior and microwave dielectric properties of CaTi1-x(Nb1/2Al1/2)xO3, Synth. Sinter. 1 (2021) 197–201. https://doi.org/10.53063/synsint.2021.1467.
[58] M. Mansoor, M. Mansoor, M. Mansoor, T. Themelis, F. Çinar Şahin, Sintered transparent polycrystalline ceramics: the next generation of fillers for clarity enhancement in corundum, Synth. Sinter. 1 (2021) 183–188. https://doi.org/10.53063/synsint.2021.1342.
[59] C.L. Gnanasagaran, K. Ramachandran, S. Ramesh, S. Ubenthiran, N.H. Jamadon, Effect of co-doping manganese oxide and titania on sintering behaviour and mechanical properties of alumina, Ceram. Int. 49 (2023) 5110–5118. https://doi.org/10.1016/j.ceramint.2022.10.027.
[60] P.A.N. Dias, N. Nasani, T.S. Horozov, D.P. Fagg, Non-aqueous stabilized suspensions of BaZr0.85Y0.15O3−δ proton conducting electrolyte powders for thin film preparation, J. Eur. Ceram. Soc. 33 (2013) 1833–1840. https://doi.org/10.1016/j.jeurceramsoc.2013.02.030.
[61] C.D. Chandler, C. Roger, M.J. Hampden-Smith, Chemical aspects of solution routes to perovskite-phase mixed-metal oxides from metal-organic precursors, Chem. Rev. 93 (1993) 1205–1241. https://doi.org/10.1021/cr00019a015.